

# PCCP

Accepted Manuscript



This is an *Accepted Manuscript*, which has been through the Royal Society of Chemistry peer review process and has been accepted for publication.

*Accepted Manuscripts* are published online shortly after acceptance, before technical editing, formatting and proof reading. Using this free service, authors can make their results available to the community, in citable form, before we publish the edited article. We will replace this *Accepted Manuscript* with the edited and formatted *Advance Article* as soon as it is available.

You can find more information about *Accepted Manuscripts* in the [Information for Authors](#).

Please note that technical editing may introduce minor changes to the text and/or graphics, which may alter content. The journal's standard [Terms & Conditions](#) and the [Ethical guidelines](#) still apply. In no event shall the Royal Society of Chemistry be held responsible for any errors or omissions in this *Accepted Manuscript* or any consequences arising from the use of any information it contains.

# Engineering of Hydrogenated Two-dimensional *h*-BN/C Superlattices as Electrostatic Substrates

Zhun Liu<sup>1</sup>, Xiaoliang Zhong<sup>2</sup>, Hui Yan<sup>1</sup> and Ru-Zhi Wang<sup>1\*</sup>

<sup>1</sup> College of Materials Science and Engineering, Beijing University of Technology, Beijing 100124, China

<sup>2</sup> Materials Science Division, Argonne National Laboratory, Lemont, Illinois 60439, USA

## Abstract

Hybridized two-dimensional materials incorporating domains from hexagonal boron nitride (*h*-BN) and graphene is an interesting branch of materials due to its highly tunable electronic properties. In the present study, we investigate the hydrogenated two-dimensional (2D) *h*-BN/C superlattices (SLs) with zigzag edges using first-principles calculations. We found that domain width, phase ratio, and vertical dipole orientation all have significant influence on the SLs' stability. The electronic reconstruction is associated with the lateral polar discontinuities at the zigzag edges and the vertical polarized  $(\text{B}_2\text{N}_2\text{H}_4)^m$  domains, which modifies the electronic structures and the spatial potential of the SLs significantly. Furthermore, we demonstrate that the hydrogenated 2D *h*-BN/C SLs can be applied in engineering the electronic structure of graphene: laterally-varying doping can be achieved by taking advantage of the spatial variation of surface potential of the SLs. By applying an external vertical electric field on this novel bidirectional heterostructures, graphene doping levels and band offsets can be tuned in a wide range, such that the graphene doping profile can be switched from the bipolar (p-n junction) to the unipolar ( $n^+$ -n junction) mode. It is expected that such bidirectional heterostructures provide an effective approach for developing novel nanoscale electronic devices and improving our understanding of the fundamentals of low-dimensional materials.

---

\*To whom correspondence should be addressed: [wrz@bjut.edu.cn](mailto:wrz@bjut.edu.cn)

**Keywords:**

Laterally-varying doping, surface potential, bidirectional heterostructures, polarization

## I. Introduction

Atomic sheets of hybridized monolayer hexagonal BN (*h*-BN) and graphene involving different domains are highly attractive for developing high-performance electronic and optoelectronic devices due to their tunable bandgap and wide mobility variation.<sup>1-3</sup> Owing to their nearly matching lattice parameters, similar crystal structures, and immiscible phase in two-dimensional (2D), the segregated domains of hybridized *h*-BN/C atomic sheets have been synthesized uniformly on large area.<sup>1,4</sup> In contrast to the two-dimensional boron-carbon-nitride (BCN) alloys, the electronic properties of the hybridized domains are strongly regulated by the domain size and their interfacial bonding.<sup>2, 5-7</sup> For instance, the 2D BN/C zigzag interfaces are half-semimetals and possess dispersive boundary states near the B-C edges, which shown that the spin asymmetric screening in graphene edges and the polarity compensation in BN domain team up to result in an electronic reconstruction at the interface.<sup>8,9</sup>

Such hybridized sheets could be extended to  $sp^3$ -bonded honeycomb analogues, like fully hydrogenated 2D BN/C heterostructures.<sup>9, 10</sup> The reversible covalently absorbed H atom on graphene and *h*-BN surface have been widely studied both experimentally and theoretically.<sup>11-13</sup> Directly solid phase hydrogenation with highly pressured  $H_2$  and exposing the pristine membranes under H plasmas are two feasible avenues to change the bonding between C (B, N) atoms from planar  $sp^2$  into tetrahedral  $sp^3$  hybridization, from which atoms in the sublattice are staggered displaced from their parent BN/C atomic plane.<sup>10-13</sup> Compared to the pristine zigzag-edged BN/C sheets, the hydrogenated *h*-BN/C heterostructures not only preserve their lateral polar discontinuities but also give rise to large variation of vertical potential gradient due to the robust vertical polarization in hydrogenated BN ( $B_2N_2H_4$ ) domains.<sup>14</sup> Therefore, it is highly desirable to study the spatial potential distributions of the hydrogenated *h*-BN/C superlattices (SLs) influenced by both of the domain size and the atomic configurations of hydrogenated graphene ( $C_4H_4$ )<sup>n</sup>

embedded in  $(\text{B}_2\text{N}_2\text{H}_4)^m$  ( $n, m$  indicate the zigzag units).<sup>6, 15, 16</sup> Most notably, these lateral heterostructures with large tunable surface potential variations can be used as the electrostatic substrates for 2D materials' spatially contrasting doping, which introduces nondegenerate doping levels due to the quantum capacitance effects in 2D materials.<sup>17-19</sup> Very recently, Park *et al.* experimentally demonstrate a widely controllable n-doping approach on a 2D transition metal dichalcogenides with the implantation of polarized dopants and dopant gradients in the substrates.<sup>20</sup> The orientation of surface dipoles influences the interfacial potential differences and, therefore, the doping levels in 2D materials. This van der Waals (vdW) interface-induced doping and band alignments can be further effectively tuned by the engineered electrostatic substrates and external electric field.<sup>21-23</sup> Therefore, when graphene is physically adsorbed on the hydrogenated 2D *h*-BN/C SLs, it is likely to tune the graphene doping profile by the local substrates underneath, for which spatial potential contrast is obtained from the polarity variations in the hydrogenated 2D *h*-BN/C SLs.<sup>14, 19</sup> Combined with external electric fields, these lateral hydrogenated 2D *h*-BN/C SLs may provide a wide range control of the electronic states of graphene by the collective electrostatic effects.<sup>3, 24, 25</sup>

In this study, based on first-principles calculations, we have investigated thermodynamic stabilities depending on domain size and electronic properties of zigzag-edged hydrogenated 2D *h*-BN/C SLs. We focus on the electronic reconstruction associated with the lateral polar discontinuities at the zigzag edges and the vertical polarized  $(\text{B}_2\text{N}_2\text{H}_4)^m$  domains. Additionally, we demonstrate that the hydrogenated 2D *h*-BN/C SLs can be used as the electrostatic substrates for graphene laterally-varying doping by taking advantage of the spatial variation of surface potential. By applying an external vertical electric field, the graphene doping levels and band offsets can be tuned in a wide range on the SLs, such that the graphene doping profile can be switched from bipolar (p-n junction) to unipolar ( $n^+$ -n junction) mode. It is expected that this field-controlled potential landscape and carrier polarity in graphene/SLs bidirectional heterostructures provide an alternative approach for

developing of novel graphene-based photodetectors and logic devices.<sup>17,26</sup>

## II. Models and methods

Two types of topology configurations are used for studying hydrogenated 2D *h*-BN/C SLs ( $Z^{(m+n) \times k} (\text{B}_2\text{N}_2\text{H}_4)^m (\text{C}_4\text{H}_4)^n dk$ ). As shown in Fig. 1, the SLs consisting of one  $(\text{B}_2\text{N}_2\text{H}_4)^m$  and one  $(\text{C}_4\text{H}_4)^n$  are suffixed by d1, i.e.  $k=1$ , while the SLs embedded with two  $(\text{B}_2\text{N}_2\text{H}_4)^m$  by reversed vertical dipole orientation are suffixed by d2, i.e.  $k=2$ . Since the d2 SLs have reversal symmetry, these supercells are two times wider than the corresponding d1 ones.  $Z^{(m+n) \times k}$  indicates  $(m+n) \times k$  zigzag units in each configuration. To investigate the domain-size-dependent stabilities and electronic properties, we mainly focus our study on the SLs constructed by equal amounts of  $(\text{B}_2\text{N}_2\text{H}_4)^m$  and  $(\text{C}_4\text{H}_4)^n$ , i.e.  $m=n$  (Fig. 1,  $Z^{2n} (\text{B}_2\text{N}_2\text{H}_4)^n (\text{C}_4\text{H}_4)^n$  d1, and  $Z^{4n} (\text{B}_2\text{N}_2\text{H}_4)^n (\text{C}_4\text{H}_4)^n$  d2). The formation energies of the structures with fixed zigzag units but varying the ratio of two phases ( $n+m=4$ , and  $1 \leq n \leq 3$ ) are also discussed and their supercells are shown in the supplementary information materials (Fig. S1,  $Z^4 (\text{B}_2\text{N}_2\text{H}_4)^{4-n} (\text{C}_4\text{H}_4)^n$  d1, and  $Z^8 (\text{B}_2\text{N}_2\text{H}_4)^{4-n} (\text{C}_4\text{H}_4)^n$  d2).

First-principles calculations are performed using Vienna ab initio Simulation Package codes (VASP) with the projector-augmented wave methods.<sup>27,28</sup> In order to accurately reveal the interlayer dispersion interactions and the electronic structure, we have used Perdew-Burke-Ernzerhof (PBE) functional combined with vdW correction proposed by Grimme (DFT-D2) for generalized gradient approximation (GGA).<sup>29</sup> The plane-wave basis with the kinetic energy cutoff, convergence criterion for energy are set at 500 eV, and  $1 \times 10^{-7}$  eV, respectively. The residue forces of hydrogenated 2D *h*-BN/C SLs are less than  $0.01 \text{ eV } \text{\AA}^{-1}$ , and that of graphene/SLs heterostructures are converged to  $0.05 \text{ eV } \text{\AA}^{-1}$ . The 2D Brillouin zone (BZ) integration is represented by  $\Gamma$ -centered Monkhorst-Pack scheme with different k-points depending on the BZ dimensions. For example, we used  $35 \times 9 \times 1$  k-points for the

$Z^4(\text{B}_2\text{N}_2\text{H}_4)^2(\text{C}_4\text{H}_4)^2$  dl electronic structural calculations. Similar sampling densities in k-space are used for other SLs and graphene/SLs heterostructures. To minimize any spurious interactions between layer images, a large vacuum layer is adopted in the c-direction (c axis length: 30 Å) perpendicular to the sheet.<sup>28</sup> The dipole correction has been included in the c-direction. We define the ac-plane (or the (x, z) plane) averaged electrostatic potential energy as a function of the y coordinate  $\bar{V}(y) = \frac{1}{A_{\text{ac-plane}}} \int dx dz V(x, z, y)$ . The lateral macroscopic average can be

defined by:  $\bar{V}(y) = \int dy' \bar{V}(y') \omega(y - y') = \frac{1}{a} \int_{y-a/2}^{y+a/2} dy' \bar{V}(y')$ , where  $\omega(y) = \frac{1}{a} \Theta(\frac{a}{2} - |y|)$ ,

$\Theta$  is the one-dimensional step function, and  $a$  is the interlayer distance along the b-axis. The concept of macroscopic average can be extended to the charge density.

### III. Results and discussion

#### (a) Structure stability of hydrogenated 2D h-BN/C SLs

The formation energies of the SLs ( $Z^{(m+n) \times k} (\text{B}_2\text{N}_2\text{H}_4)^m (\text{C}_4\text{H}_4)^n$  dk) are defined by the energy difference (per unit) between the SLs and its constituents in their respective parent phases,<sup>7</sup> i.e.,

$$E_{\text{form}} = \Delta E / [(m+n) \times k], \quad (1)$$

$$\text{where } \Delta E = E_{\text{tot}} - k \times (m \times E_{\text{B}_2\text{N}_2\text{H}_4} + n \times E_{\text{C}_4\text{H}_4}). \quad (2)$$

The  $E_{\text{tot}}$ ,  $E_{\text{B}_2\text{N}_2\text{H}_4}$ , and  $E_{\text{C}_4\text{H}_4}$  are the total energies of the SLs, ( $\text{B}_2\text{N}_2\text{H}_4$ ) and ( $\text{C}_4\text{H}_4$ ) unit, respectively.  $(m+n) \times k$  represents the amount of zigzag units in each SLs. As shown in Fig. 2, formation energy of SLs (with  $m = n$ , i.e., the solid line) decreases gradually with the increasing of  $n$ , which is similar to the reported BN/graphene zigzag SLs.<sup>7</sup> This is because the larger domains in SLs, the fewer fraction of interfacial wrong bonds (B-C and C-N) contribution to the formation energy. Therefore, the thermodynamically larger domains tend to form over the

smaller ones to lower the total energy of the system. The relative stability between the two types of configurations shows that the formation energy of d1 SLs is obviously lower than that of d2 SLs with units  $n \leq 3$ . As shown in Fig. 2, the d1 SLs is 0.16 eV less than the d2 SLs for  $n = 1$  and decreases to 0.013 eV at  $n = 4$ . Close inspection on the interface of SLs reveal that each  $(C_4H_4)^n$  domain only takes one type of interfacial bonding (either B-C or C-N) in the d2 SLs while both types of bonding are present in the d1 SLs. Therefore, the accumulation of identical polar charges at the two  $(C_4H_4)^n$  edges results in a large electrostatic repulsive energy in narrow spaces. On the contrary, in the d1 structures, both types of bonding are present at the two  $(C_4H_4)^n$  edges and generate a periodic opposite line charges, such that the Coulomb interaction energies between the charged edges of the small domains could be significantly diminished.<sup>7,8</sup>

The formation energies of SLs with fixed zigzag units but varying the ratio of two phases ( $n + m = 4$ , and  $1 \leq n \leq 3$ , i.e., the dashed lines) are also represented in Fig. 2. In this case, the formation energy is proportional to the interfacial binding energy, i.e.,

$$E_{form} = \Delta E / (4 \times k) \propto E_{bind} = \Delta E / (2 \times k). \quad (3)$$

The interfacial binding energy mainly origin from two items, i.e., the cleavage energy difference and the induced electrostatic energy.<sup>30</sup> The cleavage energy difference involves interfacial bond breaking contributions, which should be independent on the periodic width. Therefore, the potential energy differences across the  $(B_2N_2H_4)^{4-n}$  domain should have similar variation trends to their formation energies in the uncompensated electronic structure, when the built-in potentials are smaller than the bandgaps, see Fig. S2. The  $Z^4(B_2N_2H_4)^{4-n}(C_4H_4)^n$  d1 SLs with  $n = 1$  and  $n = 3$  have almost the same formation energy, which are lower than the one with  $n = 2$ . However, the formation energy of  $Z^8(B_2N_2H_4)^{4-n}(C_4H_4)^n$  d2 SLs decreases with increasing of  $n$ . As we have discussed before, because the d2 SLs possess identical charges on the two edges of  $(C_4H_4)^n$  while the d1 SLs have opposite charges, the

electrostatic potential energy would decrease when opposite charges are placed nearby but increase when identical charges are placed at adjacent locations.<sup>7, 9, 10</sup> Therefore, the d1 SLs with unequal ratio of two phases ( $n=1$ ) would have a lower formation energy than the one with equal amounts of phases ( $n=m=2$ ) due to the reduced opposite charges distances between the two edges of  $(C_4H_4)^n$ .

### (b) Electronic properties of hydrogenated 2D *h*-BN/C SLs

We next explore the electronic properties of the SLs with different configurations and periodic widths. As shown in Fig. 3(a) and 3(b) (or Fig. S3, the full band structure along the  $\Gamma$ -X-S-Y- $\Gamma$  of the whole 2D Brillouin zone), two selective SLs are used to study the band structure characters for each type of configuration, i.e.,  $Z^8(B_2N_2H_4)^4(C_4H_4)^4d1$  (a), and  $Z^8(B_2N_2H_4)^2(C_4H_4)^2d2$  (b). The real space charge densities of conduction (valance) band edge states at the  $\Gamma$  point are represented above (below) their band structures. Charge densities of the conduction band minimum (CBM) are delocalized near the C-N interface, exhibiting a 1D nearly free electrons (NFE) like dispersion. Note that the NFE mainly spill out over the N-H surface due to the vertical polarization in  $(B_2N_2H_4)^n$ .<sup>14</sup> Therefore, the NFE are distributed on both sides of the d2 SLs due to their reversal symmetry. However, charge density of valance band maximum (VBM) are mainly distributed at the B-C interfaces and decay to the nearby  $(C_4H_4)^n$ . Hence, the electron and hole carriers are highly spatially separated in the SLs, which would be desirable for photoelectric and photochemical applications.<sup>2, 9, 31, 32</sup> We further confirm that the valence band states of both SLs are contributed by the interfacial C and B  $2p_y$  orbitals (see the brown squares and green triangles on the bands). The obvious difference is the valance band of  $Z^8(B_2N_2H_4)^2(C_4H_4)^2d2$  have a large splitting near the  $\Gamma$  point, which possibly origins from the interactions between the reversed B-C bonding orbitals.<sup>6, 33</sup> We confirm this by examining the splitting energy with different SLs width. As shown in Fig. S4, the valence band splitting is about 2.61 eV for d2 SLs with  $n=1$  while

almost negligible at  $n = 4$ .

The band edge offsets of SLs with different domain width ( $1 \leq n \leq 4$ ) are shown in Fig. 3(c). VBM increases while CBM decreases with increasing  $n$  until crossing the Fermi level, which is mainly attributed to the potential-shift induced band bending.<sup>9,30</sup> The lateral polarization in  $(\text{B}_2\text{N}_2\text{H}_4)^n$  pushes up the energy levels around the B-C edges and lowers those near the N-C edges, thereby reducing the gaps. For the polarized domains above the critical width, the electrons from the top valance band transfer to the bottom of conduction band, and the system becomes metallic due to the induction of separated 1D electron and hole pockets at the interfaces. Note that conduction band starts crossing the valance band at  $n = 4$  for d1 SLs while at  $n = 2$  for d2 SLs. This indicates that the potential shift increases in both SLs begin to exceed the band gap value.<sup>30</sup> As shown in Fig. S5, the potential step in d1 SLs (1.87 eV) with  $n = 4$  is comparable to that in d2 SLs (1.89 eV) with  $n = 2$ . Although the potential steps are not the actual values due to the integral over a finite vacuum layer, the relative magnitudes can qualitatively reflect the variations of polarization charges in different domain width. For the SLs with larger  $n$ , the partially filled band edges would further accumulate 1D free charges along the interfaces and significantly affect the spatial potential distribution on the SLs.<sup>5,23</sup>

### (c) Doping of graphene by the surface potential of hydrogenated 2D *h*-BN/C SLs

The surface potential of SLs is sensitive to the laterally polarity discontinuity and the vertical polarized domains.<sup>5,9,14</sup> This large tunable surface potential could be used for 2D material spatially contrasting doping at nanoscale.<sup>19,23,25</sup> We take the bidirectional heterostructures (graphene placed on top of the SLs) as an example to explore the 2D material laterally-varying doping by the SLs. As shown in the insets of Fig. 4, the electron and hole puddles are formed at the interfaces between graphene and SLs, which indicates the amount and direction of spatially dependent charge transfer.<sup>34</sup> The local projected density of states (LDOS) along the zigzag direction of the graphene  $2p_z$  orbitals are used to estimate the local bands shift with respect to pristine graphene (see Fig. S6). For the heterostructures with d1 SLs (see Fig. 4(a)), graphene on the

C-B interface is p-type doped (the maximum is 0.23 eV) and gradually turns to n-type (the maximum is 0.63 eV) near the C-N interface. For the heterostructures with d2 SLs (see Fig. 4(b)), graphene on the C-B interface is lightly p-type doped (the maximum is 0.09 eV) and changes to highly n-type doped (maximum is 0.97 eV) on the  $(C_4H_4)^n$  domain between two C-N interfaces. The local graphene doping variations reflects the surface potential on both types of SLs significantly changes laterally. The band offset in graphene is about 0.86 eV (1.06 eV) on d1 (d2) SLs, which reveal that the induced lateral electric field of  $2.48 \times 10^8 \text{ Vm}^{-1}$  ( $2.8 \times 10^8 \text{ Vm}^{-1}$ ) occurs in graphene. Correspondingly high hot-carrier separation may be expected for graphene based p-n junctions, which makes them highly promising for broadband photodetection applications.<sup>24, 26, 35</sup>

We further explain the local doping variations by plotting the potential energy profiles of the SLs and their heterostructures with graphene, as shown in Fig. S7. The contour plots represent the relative magnitude of the potential gradient on the SLs surfaces and at the interfaces between graphene and SLs. The charge deviations at the SLs surface give rise to additional Hartree and exchange-correlation potential,<sup>22</sup> which reduce the surface potential at the electron charged region (sparse potential gradients above the C-N interface) while increase it at the hole charged region (high potential gradients above the C-B interface).<sup>9, 14</sup> Therefore, the contrast local interfacial potential and vertical dipole field between the graphene and its underneath SLs strongly influence their interface charge transfer, which result in varying degree of carbon band shifts.<sup>22, 36, 37</sup>

#### **(d) Electric field tunable graphene laterally-varying doping**

Previous studies have demonstrated that the surface potential of graphene on the substrate can be adjusted by means of electric field induced charge transfer, thereby controlling Fermi level shift of graphene.<sup>18, 23</sup> The field-effect control of the potential landscape and carrier polarity enables a wide range of new applications for graphene-based photodetectors and graphene with a graded-potential gate field-effect

transistors.<sup>17</sup> For the photodetectors, the local photocurrent density induced field and the variation of Seebeck coefficient are strongly increased near the zero carrier density.<sup>24, 26</sup> Thus, both photoelectric and photo-thermoelectric effects team up to generate a strong photoresponse near the graphene bipolar junction, allowing on-off switch of photodetection.<sup>26</sup> For the field-effect transistors with a graded-potential profile, the spatially varying electrostatic doping of graphene produces a pseudo-gap as a suppressed conductance at the zero carrier density of graphene within a controllable energy range.<sup>17</sup> The basic working principle of both types of device is using local electrostatic gate to switch between bipolar (p-n junction) and unipolar doping ( $n^+$ -n or  $p^+$ -p junction) of graphene.<sup>17, 26</sup> This inspires us to explore the electric field tunable doping mode transition in graphene with the underneath engineered SLs. For the hydrogenated 2D h-BN/C SLs, large surface potential contrast provides a laterally bipolar gating effect on the graphene. When applying an external electric field, additional field induced screen charge transfer effects would influence the graphene p-n junction, thereby changing the relative position of the graphene band. As shown in the Fig. S8, graphene doping in both types of heterostructures can be switched from bipolar to unipolar mode ( $n^+$ -n junction) under the vertical electric field.

To better understand electric field effects on switching of doping modes, 2D charge density difference contour plots of both types of heterostructures are given in Fig. 5(a)-(d). The red (blue) regions indicate electron accumulation (depletion) in the heterostructures. Compared with Fig. 5(a) and 5(c), additional charge is transferred from the bottom of  $Z^8(B_2N_2H_4)^4(C_4H_4)^4d1$  to the top surface of graphene under the vertical threshold electric field. Especially for the N-H surface below the C-N interface, the free electrons deplete significantly to screen the electric field. For the graphene adsorbed on  $Z^8(B_2N_2H_4)^2(C_4H_4)^2d2$ , the small amount of charge transfer is sufficient for the graphene to be switched to the n-type unipolar doped for its original slightly p-type doped above the B-H surface, as shown by 5(d). We integrate the charge density differences of a-c plane to reveal the charge transfer in the laterally

direction, as shown in Fig. 5(e) and 5(f). Note that both types of heterostructures have large charge redistribution along the b-axis, indicating that the laterally charge transfer is another possible approach to prompt graphene laterally varying doping. The electron-electron interactions between the graphene and SLs give response to the external perturbation by redistribution of electrons and hence a minimization of interaction energy.<sup>36</sup> Moreover, the free charges below the C-N interfaces function as a reversible electron reservoir, which make significant contributions on the graphene doping mode transition under the field. As shown in Fig. 5(e) and 5(f), the electron density near the C-N interface decreases remarkably with the increase of electric field.

The above calculations indicate that the charged zigzag interfaces in the SLs create a laterally electric field and thereby drive graphene electrons redistributing along the b-axis, which may play a significant role in graphene laterally-varying doping.<sup>9, 17</sup> Usually, the in-plane polar discontinuity generates 1D line dipoles which results a potential drop to zero following a 1/distance law. Therefore, for the SLs width larger than the carrier screening length or with arbitrary interface orientations, the Fermi level shift in graphene should be determined solely from the vertical polarization of local substrates due to the weak lateral interactions.<sup>23, 25</sup> The vertical polarized domains behavior like 2D array of dipoles arranged in a plane causes a rigid shift of the electrostatic energies. A particular example is the SLs with armchair edges and large domain widths, in which doping of graphene at each region is solely determined by the local surface dipole and the uniform vertical electric field. Therefore the laterally charge redistribution is negligible in the region far from the interface of SLs and we can perform the approximate calculations separately.

As shown in Fig. 6(a), graphene is p-type doped on the B-H surface, and n-type doped on the C-H surface and N-H surface. The band alignments imply that the graphene p-n junction can be achieved by changing the local substrates from B-H surface to C-H surface and then to N-H surface. Furthermore, graphene on the local surface of SLs shows different electric-field-dependent variation of doping. As can be seen from the Fig. 6(b), graphene doping by the local substrates show field tunability in the order of B-H surface > C-H surface > N-H surface. This diverse response of

graphene doping to external electric field are rooted in the difference of the screening effects of the substrates.<sup>18,36</sup> The larger amount of free electrons on the N-H surface can screen external electric field and hence limit the field-induced charge transfer.<sup>23,26</sup> On the other hand, the lightly n-type doped graphene on C-H surface can be easily tuned to be charge neutral by the negative-bias field. For the higher negative field applied, there is no charge transfer between the layers due to the Fermi level pinned at the Dirac point energy in the bandgap of substrate, tuning this contact into a Schottky one. Hence, the Schottky barrier height between the C-H surface and graphene can be further tuned.<sup>21</sup> Such electric-field-dependent variation of graphene local doping and Schottky barrier height on the engineered SLs substrate provide a large tunability of band offsets for graphene p-n or n<sup>+</sup>-n junctions.

#### IV. Conclusions

In summary, we have investigated the hydrogenated 2D *h*-BN/C SLs with zigzag edges by means of first-principles calculations. We found that domain width, phase ratio, and vertical dipole orientation all have significant influence on the SLs' stabilities. The electronic reconstruction in (B<sub>2</sub>N<sub>2</sub>H<sub>4</sub>)<sup>*m*</sup> domains is associated with the lateral polar discontinuities at the zigzag edges and the vertical polarizations, which modifies the band structure and the spatial potential of the SLs significantly. We have further demonstrated that the hydrogenated 2D *h*-BN/C SLs can be used as the electrostatic substrates for graphene laterally-varying doping by taking advantage of the spatial variation of surface potential. A shift of the local electronic states of the graphene 2p<sub>z</sub> orbitals with respect to the Fermi level was achieved. By applying an external vertical electric field, graphene doping levels and band offsets can be tuned in a wide range, such that the graphene doping profile can be switched from bipolar (p-n junction) to unipolar (n<sup>+</sup>-n junction) mode in this novel bidirectional heterostructures. It is indicated that engineering of laterally SLs to control the surface potential provide an effective approach for 2D materials spatially contrasting doping,

thereby contributing to the development of novel nanoscale electronic devices and improving our understanding of the fundamentals of low-dimensional materials.

### **Acknowledgements**

The work was financially supported by the National Natural Science Foundation of China (NSFC) (Grant Nos. 51472010 and 11274029), the Jing-Hua Talents Project of Beijing University of Technology (No. 2014-JH-L07), the Foundation on the Creative Research Team Construction Promotion Project of the Beijing Municipal Institution (No. IDHT20140506) and the Importation and Development of High-Caliber Talents Project of the Beijing Municipal Institutions (No. CIT&TCD201204037).

## References

1. L. Ci, L. Song, C. Jin, D. Jariwala, D. Wu, Y. Li, A. Srivastava, Z. F. Wang, K. Storr, L. Balicas, F. Liu and P. M. Ajayan, *Nat. Mater.*, 2010, **9**, 430-435.
2. M. Bernardi, M. Palummo and J. C. Grossman, *Phys. Rev. Lett.*, 2012, **108**, 226805.
3. Q. Zeng, H. Wang, W. Fu, Y. Gong, W. Zhou, P. M. Ajayan, J. Lou and Z. Liu, *Small*, 2015, **11**, 1868-1884.
4. M. P. Levendorf, C. J. Kim, L. Brown, P. Y. Huang, R. W. Havener, D. A. Muller and J. Park, *Nature*, 2012, **488**, 627-632.
5. J. Park, J. Lee, L. Liu, K. W. Clark, C. Durand, C. Park, B. G. Sumpter, A. P. Baddorf, A. Mohsin, M. Yoon, G. Gu and A. P. Li, *Nat. Commun.*, 2014, **5**, 5403.
6. J. Jung, Z. Qiao, Q. Niu and A. H. MacDonald, *Nano Lett.*, 2012, **12**, 2936-2940.
7. S. Jungthawan, S. Limpijumnong and J.-L. Kuo, *Phys. Rev. B*, 2011, **84**, 235424.
8. J. M. Pruneda, *Phys. Rev. B*, 2010, **81**, 161409.
9. M. Gibertini, G. Pizzi and N. Marzari, *Nat. Commun.*, 2014, **5**, 5157.
10. F. W. Averill, J. R. Morris and V. R. Cooper, *Phys. Rev. B*, 2009, **80**, 195411.
11. C. Tang, Y. Bando, X. Ding, S. Qi and D. Golberg, *J. Am. Chem. Soc.*, 2002, **124**, 14550-14551.
12. S.-P. Chan, G. Chen, X. Gong and Z.-F. Liu, *Phys. Rev. Lett.*, 2001, **87**, 205502.
13. D. C. Elias, R. R. Nair, T. M. G. Mohiuddin, S. V. Morozov, P. Blake, M. P. Halsall, A. C. Ferrari, D. W. Boukhvalov, M. I. Katsnelson, A. K. Geim and K. S. Novoselov, *Science*, 2009, **323**, 610-613.
14. Z. Liu, R.-Z. Wang, L.-M. Liu, W.-M. Lau and H. Yan, *PCCP*, 2015, **17**, 11692-11699.
15. Y. Xie, H. Yu, H. Zhang and H. Fu, *PCCP*, 2012, **14**, 4391-4397.
16. P. Gori, O. Pulci, M. Marsili and F. Bechstedt, *Appl. Phys. Lett.*, 2012, **100**, 043110.
17. X. Wang, X. Jiang, T. Wang, J. Shi, M. Liu, Q. Zeng, Z. Cheng and X. Qiu, *Nano Lett.*, 2015, **15**, 3212-3216.
18. S. Tang, J. Yu and L. Liu, *PCCP*, 2013, **15**, 5067-5077.
19. S. Behura and V. Berry, *ACS Nano*, 2015, **9**, 2227-2230.
20. H.-Y. Park, M.-H. Lim, J. Jeon, G. Yoo, D.-H. Kang, S. K. Jang, M. H. Jeon, Y. Lee, J. H. Cho, G. Y. Yeom, W.-S. Jung, J. Lee, S. Park, S. Lee and J.-H. Park, *ACS Nano*, 2015, **9**, 2368-2376.
21. J. Padilha, A. Fazzio and A. J. da Silva, *Phys. Rev. Lett.*, 2015, **114**, 066803.
22. J. Gebhardt, F. Viñes and A. Görling, *Phys. Rev. B*, 2012, **86**, 195431-119546.
23. H. Y. Chiu, V. Perebeinos, Y. M. Lin and P. Avouris, *Nano Lett.*, 2010, **10**, 4634-4639.
24. F. H. L. Nature Physics Koppens, T. Mueller, P. Avouris, A. C. Ferrari, M. S. Vitiello and M. Polini, *Nat. Nanotechnol.*, 2014, **9**, 780-793.
25. W. Zhu, H. Chen, K. H. Bevan and Z. Zhang, *ACS Nano*, 2011, **5**, 3707-3713.
26. M. C. Lemme, F. H. L. Koppens, A. L. Falk, M. S. Rudner, H. Park, L. S. Levitov and C. M. Marcus, *Nano Lett.*, 2011, **11**, 4134-4137.
27. G. Kresse and J. Furthmüller, *Phys. Rev. B*, 1996, **54**, 11169-11186.
28. G. Makov and M. C. Payne, *Phys. Rev. B*, 1995, **51**, 4014-4022.
29. S. Grimme, *J. Comput. Chem.*, 2006, **27**, 1787-1799.

30. C. Noguera and J. Goniakowski, *J. Phys.: Condens. Matter*, 2008, **20**, 264003.
31. S. Ida, A. Takashiba, S. Koga, H. Hagiwara and T. Ishihara, *J. Am. Chem. Soc.*, 2014, **136**, 1872-1878.
32. Z. Liu, R.-Z. Wang, L.-M. Liu, H. Yan and W.-M. Lau, *J. Mater. Chem. A*, 2014, **2**, 9744-9750.
33. R. Drost, A. Uppstu, F. Schulz, S. K. Hämäläinen, M. Ervasti, A. Harju and P. Liljeroth, *Nano Lett.*, 2014, **14**, 5128-5132.
34. J. Martin, N. Akerman, G. Ulbricht, T. Lohmann, J. H. Smet, K. von Klitzing and A. Yacoby, *Nat. Phys.*, 2007, **4**, 144-148.
35. J. Cai, C. A. Pignedoli, L. Talirz, P. Ruffieux, H. Söde, L. Liang, V. Meunier, R. Berger, R. Li, X. Feng, K. Müllen and R. Fasel, *Nat. Nanotechnol.*, 2014, **9**, 896-900.
36. L. Matthes, K. Hannewald, J. Furthmüller and F. Bechstedt, *Phys. Rev. B*, 2011, **84**, 115427.
37. S. Yang, P. Zhou, L. Chen, Q. Sun, P. Wang, S. Ding, A. Jiang and D. W. Zhang, *J. Mater. Chem. C*, 2014, **2**, 8042-8046.

**Figure captions:**

Fig. 1. Optimized structures of hydrogenated 2D *h*-BN/C zigzag edged SLs with equal amounts of  $(\text{B}_2\text{N}_2\text{H}_4)^m$  and  $(\text{C}_4\text{H}_4)^n$ , (i.e.  $m = n$ ), where  $m$ ,  $n$  indicate the zigzag units of the domain widths. The top views are indicated by the  $b$  and  $a$  axes ( $b$ , and  $c$  axis for lateral views). The dashed lines show the repetition of the boundary conditions. The SLs consisting of one  $(\text{B}_2\text{N}_2\text{H}_4)^m$  and one  $(\text{C}_4\text{H}_4)^n$  are shown in the upper panel, ( $Z^{2n}(\text{B}_2\text{N}_2\text{H}_4)^n(\text{C}_4\text{H}_4)^n \text{d1}$ ), and the SLs embedded with two  $(\text{B}_2\text{N}_2\text{H}_4)^m$  by reversed vertical dipole orientation are represented in the bottom panel ( $Z^{4n}(\text{B}_2\text{N}_2\text{H}_4)^n(\text{C}_4\text{H}_4)^n \text{d2}$ ).

Fig. 2. The domain-size-dependent formation energy (per zigzag unit) of each configuration refers to its parent phases. The dashed lines represent the configurations with fixed zigzag units but varying the ratio of two phases ( $m + n = 4$ ,  $1 \leq n \leq 3$ ).

Fig. 3. Electronic properties of the SLs (with  $m=n$ ). Band structures (X-direction corresponds to the direction along a-axis) for  $Z^8(\text{B}_2\text{N}_2\text{H}_4)^4(\text{C}_4\text{H}_4)^4\text{d1}$  (a), and  $Z^8(\text{B}_2\text{N}_2\text{H}_4)^2(\text{C}_4\text{H}_4)^2\text{d2}$  (b). The charge density distributions of the conduction (valence) band edge states are presented above (below) their band structure diagrams (plotting isosurface is  $8 \times 10^{-4} e\text{\AA}^{-3}$ ). The contributions of interfacial B and C atoms  $2p_y$  orbitals to the bands are colored with brown squares and green triangles, respectively. (c) The alignments of band edge offsets for the two types of SLs with different zigzag units ( $1 \leq n \leq 4$ ). The energy levels of d1 (d2) SLs are represented by the left thin (right thick) frame bars, respectively. The black (red) frame heights show the energy level spacings between the Fermi level and CBM (VBM), and the inset is the enlarged frame bars for  $Z^{2n}(\text{B}_2\text{N}_2\text{H}_4)^n(\text{C}_4\text{H}_4)^n\text{d1}$  with  $n = 3, 4$ . The energy level spacings under the Fermi level are represented by shadows.

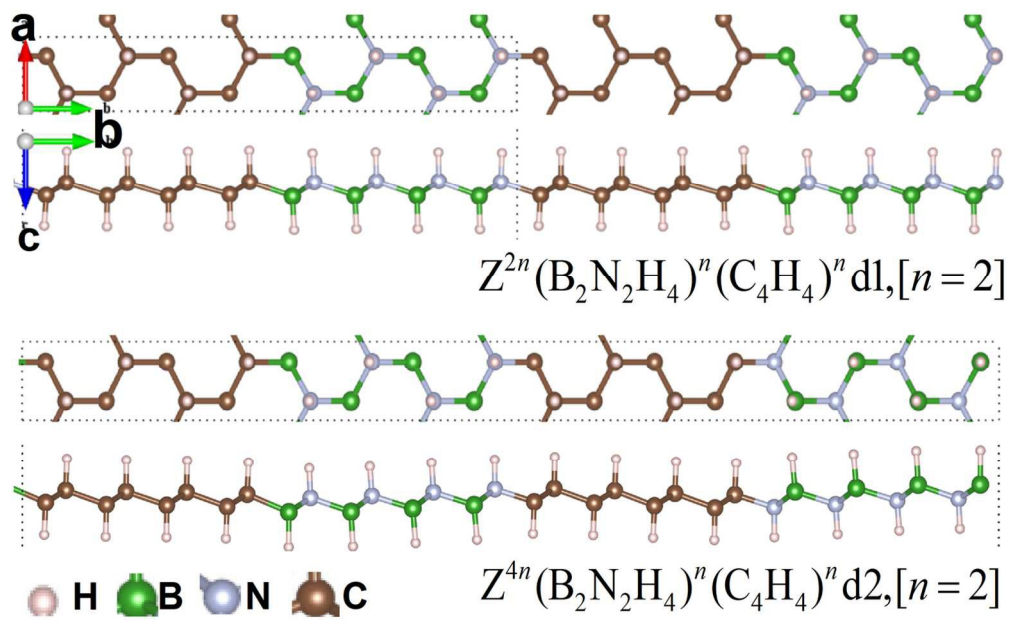
Fig. 4. Graphene doped by SLs of  $Z^8(\text{B}_2\text{N}_2\text{H}_4)^4(\text{C}_4\text{H}_4)^4\text{d1}$  (a), and  $Z^8(\text{B}_2\text{N}_2\text{H}_4)^2(\text{C}_4\text{H}_4)^2\text{d2}$  (b). The local projected density of states (LDOS) of the carbon  $2p_z$  orbital in graphene (along 8 zigzag units from bottom to top, as shown in the insets). Two vertical lines near the Fermi level (dashed lines) represent the positions of Van Hove singularities (VHs) in pristine graphene. The pseudogap between the two VHs is marked with color box. The magenta (cyan) color indicates the local carbon  $2p_z$  states down (up) shift with respect to pristine graphene. The charge density differences of the graphene/SLs  $\Delta\rho = \rho_{\text{tot}} - \rho_{\text{SLs}} - \rho_{\text{graphene}}$  are shown in the insets with isosurface of  $1 \times 10^{-3} e\text{\AA}^{-3}$ . The orange (green) color indicates charge accumulation (depletion).

Fig. 5. Contour plots of 2D charge density difference of graphene adsorbed on top of SLs  $Z^8(\text{B}_2\text{N}_2\text{H}_4)^4(\text{C}_4\text{H}_4)^4\text{d1}$  (a), and  $Z^8(\text{B}_2\text{N}_2\text{H}_4)^2(\text{C}_4\text{H}_4)^2\text{d2}$  (b), and the corresponding contour plots for the heterostructures with doping mode transition under the threshold electric fields (c), and (d), respectively. The red (blue) contour lines are represented for positive (negative) values, and the largest positive and negative values are depicted in the inset with unit of  $e\text{\AA}^{-3}$ . The contour step is set to 1/16 of the range in each plot. The macroscopic averaged integrated charge density difference (along b axis) of the heterostructures under different electric fields with graphene adsorbed on top of  $Z^8(\text{B}_2\text{N}_2\text{H}_4)^4(\text{C}_4\text{H}_4)^4\text{d1}$  (e) and  $Z^8(\text{B}_2\text{N}_2\text{H}_4)^2(\text{C}_4\text{H}_4)^2\text{d2}$  (f).

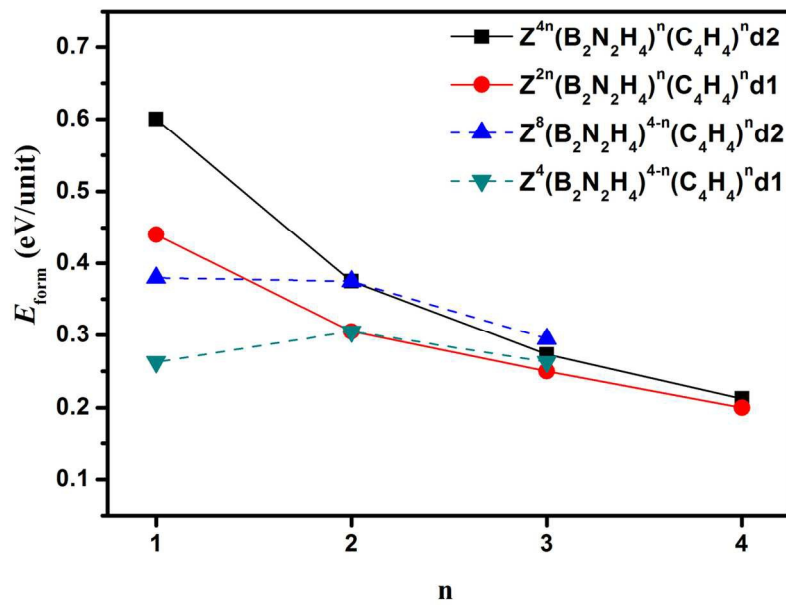
Fig. 6. (a) Schematic diagrams showing band alignments between graphene and local substrates, (left) on B-H surface, (middle) on C-H surface, and (right) on the N-H surface. The horizontal green (orange) lines represent the VBM (CBM) of the local substrates. The crossed lines indicate the Dirac cone of the graphene. (b) Dirac point shifts as a function of the electric field for the graphene on three types of substrates.

TOC Figure:

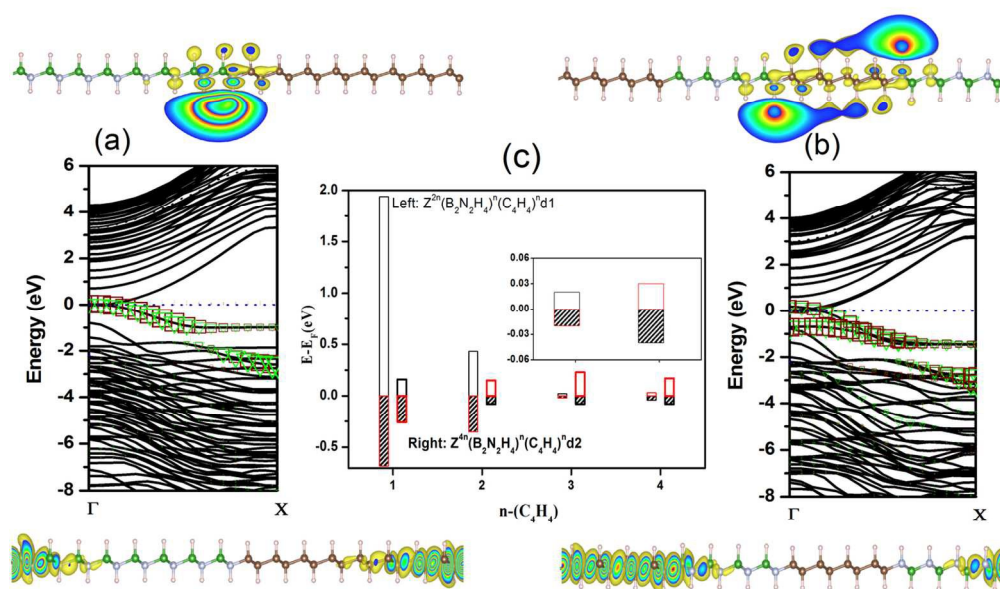
Engineering of hydrogenated two-dimensional h-BN/C superlattices as electrostatic substrates for graphene laterally varying doping



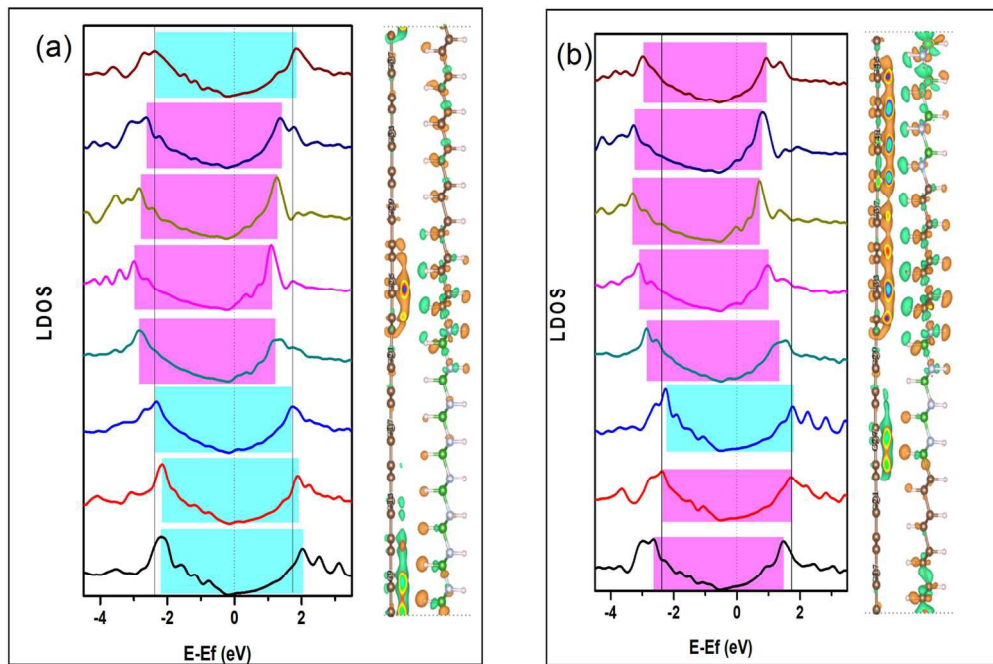
131x84mm (300 x 300 DPI)



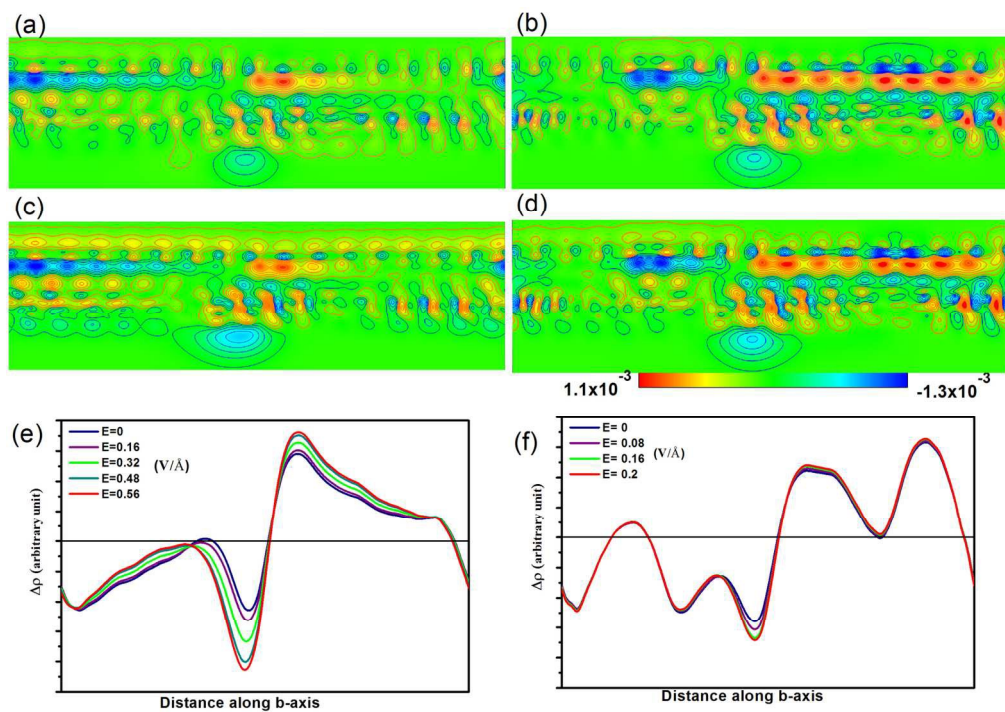
142x100mm (300 x 300 DPI)



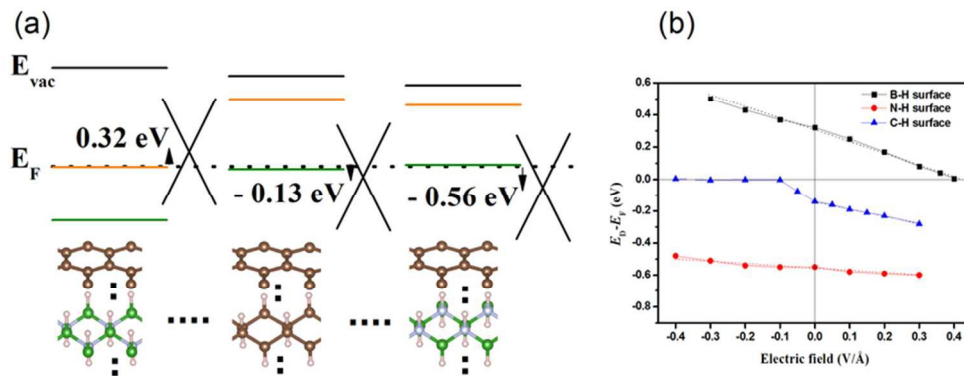
127x79mm (300 x 300 DPI)



135x90mm (300 x 300 DPI)



144x103mm (300 x 300 DPI)



76x28mm (300 x 300 DPI)